# Geological Magazine

## www.cambridge.org/geo

# **Original Article**

Cite this article: Palei RR, Gupta AK, Sanyal P, and Jaiswal MK. Geochemical and microtextural properties of pyritized foraminiferal tests: results from ODP hole 763A, Southeastern Indian Ocean. *Geological Magazine* 162(e44): 1–16. https://doi.org/10.1017/S0016756825100307

Received: 31 January 2025 Revised: 25 September 2025 Accepted: 26 September 2025

#### **Keywords:**

Fe-S coatings; anoxic; diagenesis; framboidal pyrite; Southeastern Indian Ocean

#### Corresponding author:

Anil Kumar Gupta; Emails: anil\_k\_gupta1960@yahoo.co.in, anilg@gg.iitkgp.ac.in

© The Author(s), 2025. Published by Cambridge University Press. This is an Open Access article, distributed under the terms of the Creative Commons Attribution licence (https://creativecommons.org/licenses/by/4.0/), which permits unrestricted re-use, distribution and reproduction, provided the original article is properly cited.



# Geochemical and microtextural properties of pyritized foraminiferal tests: results from ODP hole 763A, Southeastern Indian Ocean

Rina Rani Palei<sup>1</sup>, Anil Kumar Gupta<sup>1</sup>, Prasanta Sanyal<sup>2</sup> and Manoj Kumar Jaiswal<sup>2</sup>

<sup>1</sup>Department of Geology and Geophysics, Indian Institute of Technology Kharagpur, Kharagpur, India and <sup>2</sup>Department of Earth Sciences, Indian Institute of Science Education and Research (IISER) Kolkata, Mohanpur, India

#### Abstract

The pyritization of microfossils serves as a key indicator of paleoenvironmental conditions, yet the controlling factors on pyrite morphology and composition remain poorly constrained. This study encountered different pyrite morphology (framboids and patches) from the foraminiferal tests retrieved from the marine sediment samples of Ocean Drilling Program Hole 763A, southeastern Indian Ocean, during different geological time slices. We hypothesize that distinct microenvironments and controlling factors might have influenced the morphology. Detailed investigations of the morphology, mineralogy and geochemistry of Fe-S coatings within and on foraminiferal tests suggest the dynamics of paleoredox conditions during the Middle Pleistocene and Upper Miocene. The comprehensive geochemical overview and the presence of Ni and Ba associated with Fe-S coatings and sediments suggest deoxygenation of deep-sea sediments driven by climatic shifts rather than hydrothermal activities. The stable anoxic deep ocean setting during the Middle Pleistocene, evidenced by increased organic matter flux and ocean stratification, contributed to low bottom-water oxygen levels. The geochemical evidence from the Upper Miocene samples indicates predominantly oxidising conditions, as shown by the altered reddish-yellow foraminiferal tests, which are mainly composed of calcite. However, localized reducing conditions are evidenced by patches of pyrite associated with foraminiferal shells, suggesting the presence of transitional redox conditions within the oxidising sediments during the Upper Miocene.

#### 1. Introduction

Marine sediments, including the well-preserved fossilized remains, provide a primary archive from which these proxies are derived, making them invaluable for reconstructing past ocean conditions. Pyrite is widely distributed in marine sediments, and its morphology has been extensively documented, making it a reliable proxy for reconstructing the redox conditions of bottom waters and basinal redox history (Chang *et al.* 2022; Emmings *et al.* 2022). Pyritization of microfossils occurs through the authigenic formation of pyrite (FeS<sub>2</sub>) via bacterial sulphate reduction in anoxic settings, where hydrogen sulphide (H<sub>2</sub>S) reacts with reactive iron within shells (Buckman *et al.* 2020). Pyrite formation depends on organic matter, H<sub>2</sub>S and the availability of reactive detrital iron (Chen *et al.* 2021; Chang *et al.* 2022). In terrigenous marine sediments, iron is typically abundant and reactive enough, allowing pyrite formation without limitation, while highly calcareous sediments contain very little iron compared to terrigenous input (Berner, 1984). Additionally, in freshwater sediments, low sulphate concentrations restrict pyrite formation, resulting in minimal pyrite and a weak correlation with organic carbon (Raiswell *et al.* 2018).

The process of fossil pyritization in natural deep-sea sediments is influenced by a complex interplay between environmental and depositional factors. These include the composition of the sediment, organic matter availability (associated with productivity, which can control the subsurface oxygen consumption), the availability of reactive iron (the source of Fe and other redox-sensitive elements) and the oxygenation of the bottom water (ocean circulation can control the ventilation of deep water) (Berner, 1984; Poulton *et al.* 2004; Hoogakker *et al.* 2025). Together, these factors drive the formation, abundance and morphology of pyrite within microfossils, providing insights into the microenvironmental condition that may have contributed to the basin-wide anoxia and localized redox. Diverse pyrite morphology records fine-scale microenvironmental shifts driven by organic matter supply, microbial sulphate reduction and bottom-water redox conditions (Wignall *et al.* 2005; Chang *et al.* 2022; Wang *et al.* 2023). Framboids are the most abundant and common mineral texture in pyrite (Rickard, 2021). Previous studies suggest that the framboid size distribution described by multiplicative statistical parameters can be used as a probe for the oxygenation state of the paleo-environment (Wilkin *et al.* 1996; Rickard, 2019; Lee *et al.* 2024). In the Black Sea, for example, small framboids

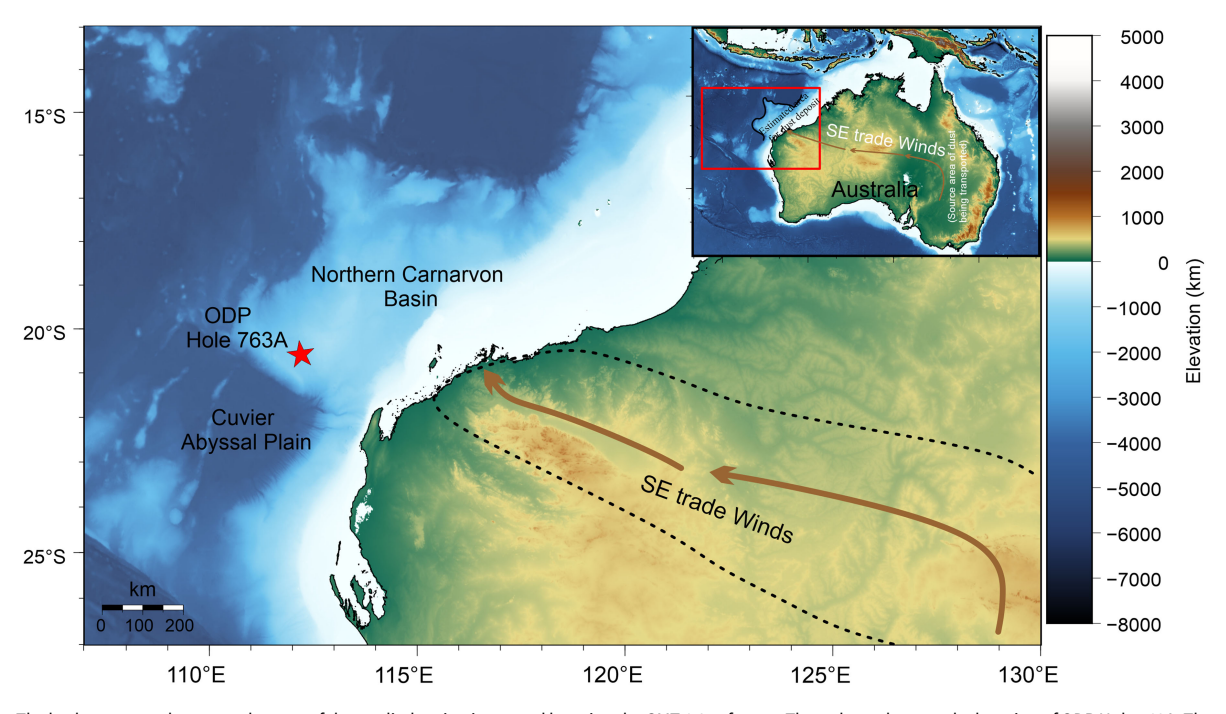


Figure 1. The bathymetry and topography map of the studied region is created by using the GMT 6.0 software. The red star denotes the location of ODP Hole 763A. The wind path, source area and estimated dust deposition region are illustrated here based on the findings of Karp et al. (2020).

reflect rapid growth within the euxinic water column, whereas larger framboids indicate slower formation within sulphidic sediments (Wilkin *et al.* 1997).

The main objective of this work is to examine the potential drivers of foraminiferal pyritization to better constrain episodes of anoxia in the southeastern Indian Ocean, a setting characterized by the pulses of consistent upwelling and persistent oxygen minimum zones (OMZs). In this study, we integrate scanning electron microscope (SEM) and energy-dispersive X-ray spectroscopy (EDS) analyses with a suite of geochemical investigations to examine the microenvironmental factors controlling the diverse Fe-S morphologies associated with foraminiferal tests. The morphological evidence of pyrite from the foraminiferal tests, such as the coatings and framboidal textures, highlights differences in preservation states and offers insights into small-scale changes in the environments during the diagenesis. The methodological framework established in this study is anticipated to be beneficial for the analysis of other pyritized microfossils and pyrite-rich mudstones across different geological basins.

# 2. Location and geological setting of the study area

Ocean Drilling Program (ODP) Hole 763A is located on the western part of the central Exmouth Plateau, offshore NW Australia in the southeastern Indian Ocean (lat. 20° 35.19′ S; long. 112° 12.52′ E; water depth 1367.5 m) (Fig. 1). The Exmouth Plateau was characterized by a broad zone of continental crust that underwent extensive deformation during Jurassic rifting, followed by early Cretaceous seafloor spreading in the adjacent Indian Ocean (Lorenzo et al. 1991; Gibbons et al. 2012). Seismic and gravity data across the southern margin of the plateau reveal a complex crustal structure shaped by two main tectonic phases (Stagg & Colwell, 1994). The structural and magmatic evolution of the southern margin of the Exmouth Plateau offers insight into the processes that shape continent-ocean transform boundaries (Lorenzo et al. 1991).

Additionally, the region is well-known for its significant hydrocarbon potential (Haq & von Rad, 1990). Hole 763A was drilled to a total depth of 1036.6 metres below the sea floor (mbsf) with a relatively high core recovery rate of 82%. The upper 141.7 m consists of grey to white early Miocene to Quaternary foraminiferal nannofossil oozes. Sediments at Hole 763A were neither heated (Snowdon & Meyers, 1992) nor exposed to high-temperature fluids during burial (Haq & von Rad, 1990). The Southeast (SE) trade winds carry dust that impacts the sediments at Hole 763A (Karp *et al.* 2021).

# 3. Samples and methods

# 3. a. Chronology

Age determination for each sample was conducted using 14 chron and subchron boundaries as age control points (Haq & von Rad, 1990) (Table 1). To ensure precision, these ages have been aligned with the updated geological time scale of Raffi *et al.* (2020) (Table 1). The interpolated ages for each sample analyzed are given in Table 2.

## 3. b. Sample preparation

The sediment core samples were processed in the Sample Processing Unit of the Palaeoceanography and Palaeoclimatology Laboratory, Department of Geology and Geophysics, IIT Kharagpur, following the standard procedure outlined by Gupta & Thomas (2003). Each sediment sample was soaked in water for eight to ten hours, with a half spoon of sodium bicarbonate and ~1-2 drops of diluted hydrogen peroxide (2%) added, which helped to disaggregate samples effortlessly. The soaked samples were then washed over a 63  $\mu$ m-sized sieve using a jet of water to eliminate clay-sized particles. To prevent contamination, the sieve was stained with a methylene blue solution after each wash. The wet samples were then dried at approximately 50°C in an electric oven, and the dried samples were stored in labelled glass vials. The dry samples were then sieved using a sieve with a mesh size greater than 149  $\mu$ m and

Table 1. Age datums are based on chron and subchron paleomagnetic boundaries established by Haq & von Rad (1990) and further updated to Raffi et al. (2020)

Sl. No	ODP Hole	Depth (mbsf)	Datums	Age (Ma)
1	763A	15.1	Brunhes/Matuyama Boundary	0.78
2	763A	18.3	Top of Jaramillo (N)	0.98
3	763A	21.1	Base of Jaramillo (N)	1.07
4	763A	31.1	Top of Olduvai (N)	1.77
5	763A	35.7	Base of Olduvai (N)	1.94
6	763A	45.8	Top of Reunion (N)	2.15
7	763A	52.3	Matuyama/Gauss Boundary	2.58
8	763A	64.2	Top of Kaena (R)	3.032
9	763A	67.8	Top of Mammoth (R)	3.207
10	763A	81.5	Gauss/Gilbert Boundary	3.596
11	763A	90.1	Base of Cochiti (N)	4.3
12	763A	94.5	Top of Sidufjall (N)	4.799
13	763A	99.5	Top of Thevra (N)	4.997
14	763A	107.9	Base of Gilbert	6.023

Table 2. Interpolated ages of analyzed samples from ODP Hole 763A

Sl. NO	Leg	Sample source	Depth (mbsf)	Age (Ma)
1	122	763A, 2H-7W, 5–7.0 cm	13.96	0.721
2	122	763A, 3H-2W,100-102cm	16.91	0.898
3	122	763A, 3H-5W, 53–55.0 cm	20.94	1.065
4	122	763A, 13H-3W, 100–102 cm	113.41	6.581
5	122	763A, 13H-5W, 5–7 cm	115.46	6.786

were evenly distributed on a black metal tray, and the well-preserved foraminiferal tests exhibiting pyrite coatings were picked up by a stable brush under a stereozoom microscope.

To explore the microscale morphological characteristics of pyrite, the tests were ultrasonically cleaned with Milli-Q water to remove any adhering particles for analysis using the SEM. Polished thin sections were prepared from the sediment core samples using resin impregnation to fill larger pores and stabilize the specimens. Once affixed to glass slides, the samples were machine-polished to a thickness of 30 µm using a 600-grade aluminium oxide slurry. The polished thin sections were then cleaned in an ultrasonic bath with methanol to eliminate any residual polishing agents. Prior to SEM analysis, the thin sections and individual tests were carboncoated. From the middle Pleistocene, planktic foraminiferal species such as Trilobatus quadrilobatus and Globorotalia hirsuta and the benthic foraminifer Bulimina striata were used for SEM, while coatings found on the surfaces of tests of the planktic foraminifera Neogloboquadrina humerosa, Sphaeroidinellopsis seminulina and Dentoglobigerina altispira were used from the Upper Miocene.

## 3. c. Analytical methods

# 3. c.1. SEM-EDS analysis and size measurement of pyrite framboids

Images were obtained using a JEOL JSM 6490 SEM at the Department of Geology and Geophysics, IIT Kharagpur, operating at an acceleration voltage of 20 kV and a working

distance of 12 mm. The SEM was equipped with backscattered electron detectors, along with EDAX (JEOL) and INCA (Oxford) EDS units, which were utilized to characterize the semi-quantitative elemental composition of individual specimens and layers. The analytical conditions for EDS X-ray elemental mapping included a frame duration of 82.8 seconds, map dwell times of 1555  $\mu s$  and a line scan dwell time of 2000  $\mu s$ , with a spectrum acquisition time of 20 seconds and a line scan resolution of 256  $\times$  208 pixels. The SEM images were captured under both backscattered electron (BSE) and secondary electron (SE) conditions for both polished thin sections and individual specimens.

The pyrite morphologies were examined under SEM, and the sizes of the pyrite framboids were measured through image analysis using ImageJ software. A pyrite framboid was measured when its morphological features matched the established definition of framboidal texture (Ohfuji and Rickard, 2005), which includes a spheroidal to sub-spheroidal shape, an aggregation of individual pyrite microcrystals and a consistent morphology and size characteristic of pyrite microcrystals. Following Rickard (2019), the number of framboids measured per sample ranged from 30 to 202. In this study, a total of 280 framboids were measured from the middle Pleistocene samples, while 92 framboids were measured from the Upper Miocene samples. To better analyze the data sets, some multiplicative parameters, such as the geometric mean and the geometric standard deviation, are used.

#### 3. c.2. Micro-Raman spectroscopy

Raman spectral analysis was performed to identify the minerals present in foraminiferal tests and their authigenic coatings. Raman spectra were obtained from eight points from six individual specimens with coatings using a Horiba LabRAM HR Evolution spectrometer, which is equipped with a multichannel Peltier-cooled (–70°C) CCD detector and a 532 nm frequency-doubled Nd: YAG laser. The analysis was conducted with a spectral resolution of 3 cm<sup>-1</sup> and a spectral range of 100–2000 cm<sup>-1</sup>. Acquisitions were performed with a 30-second exposure time and 25% laser power to enhance the signal-to-noise ratio while minimising fluorescence, conducted at the Central Research Facility Centre, IIT Kharagpur.

# 3. c.3. X-ray diffraction (XRD)

Three dried samples, free of carbonate and organic matter, were powdered and homogenized using an agate mortar. The powdered samples were analyzed via XRD using an Empyrean PANalytical diffractometer equipped with a PIXcel3D detector and a copper radiation source (Cu K $\alpha$ ,  $\lambda=0.15$  nm) across a 20 range of 5–80°. The raw XRD data were processed with PANalytical High Score software (version 3.0.5) to identify the major mineral phases, and background correction was conducted using OriginLab software.

# 3. c.4. Stable oxygen and carbon isotope analyses of carbonate

Stable carbon ( $\delta^{13}$ C) and oxygen ( $\delta^{18}$ O) isotope analyses were performed on calcite tests of benthic foraminifer *Cibicides wuellerstorfi* and planktic foraminifer *Trilobatus sacculifer* from five samples. The measurements were conducted using a Finnigan MAT-253 Isotope Ratio Mass Spectrometer, coupled with a Kiel-IV automated carbonate preparation device at IISER Kolkata. To ensure reproducibility, international standards IAEA-603 ( $\delta^{13}$ C: 2.4 ‰,  $\delta^{18}$ O: -2.4 ‰) were analyzed in conjunction with an internal laboratory standard, Z-Carrara ( $\delta^{13}$ C: 2.2 ‰,  $\delta^{18}$ O: -1.3 ‰). The standard deviation of the  $\delta^{13}$ C and  $\delta^{18}$ O values for IAEA-603 is ±0.01 and ± 0.01 (n=1, 1 $\sigma$ ), respectively, and for Z-Carrara is ±0.01 and ± 0.01 (n=1, 1 $\sigma$ ), respectively. The results are reported relative to the Vienna Pee Dee Belemnite (VPDB).

# 3. c.5. X-ray fluorescence (XRF) analysis

We employed the fused bead method for XRF analysis. Each sample was finely crushed, weighing 0.64 g and combined with 2.22 g of lithium metaborate, 4.14 g of lithium tetraborate (composed of 65%  $\text{Li}_2\text{B}_4\text{O}_7$  and 35% LiBO<sub>2</sub>) and 0.5% lithium bromide. A 7-gram mould was prepared for each sample, maintaining a flux ratio of 1:10. Utilising the xrFuse2 Electric Automatic Fusion Furnace, the samples were melted at 1100°C, followed by shaking and cooling. This procedure converted the pulverized samples into glass beads, with each sample taking 23 minutes to complete the process (Upadhyay et al. 2021). Major elemental analysis was conducted using XRF (Bruker S8 Tiger, Germany) at the Indian Institute of Science Education and Research Kolkata. Calibration was performed using standard reference materials, including JSD1 and JLK1 (Imai et al. 1996). Analytical error (standard deviation\*100/average) for repeated samples of Al<sub>2</sub>O<sub>3</sub> (%), CaO (%), Fe<sub>2</sub>O<sub>3</sub> (%), K<sub>2</sub>O (%), MgO (%), Na<sub>2</sub>O (%), P<sub>2</sub>O<sub>5</sub> (%), SiO<sub>2</sub> (%), TiO<sub>2</sub> (%) and MnO (%) ranges from 0 to 2.32%.

#### 4. Results

# 4. a. Morphology and micro-textures of pyrite that appear to coat or infill foraminiferal tests

At the studied location, benthic foraminifera are very rare, whereas planktic foraminifera are abundant throughout the studied sequence. Both planktic foraminifera (including mixed-layer and thermocline dwellers) and benthic foraminifera (epifauna and infauna) show evidence of pyritization. In the middle Pleistocene samples, ~30%-40% of foraminiferal specimens from an aliquot of 1/128 show signs of pyritization as observed under a microscope. Some tests appear dark and uniformly filled (Figs. 2A, B), while a broken test reveals the dark pyrite filling (Fig. 2C). In the Upper Miocene samples, it has been observed that ~25%-30% of the total foraminiferal specimens exhibit a patchy appearance. Black patches appear to coat or cover the shells of foraminifera (Fig. 2D), contrasting with the more extensive infilling seen in the middle Pleistocene samples. Broken shells reveal that some chambers appear to be partially coated or covered, rather than completely filled with Fe-S deposits (Fig. 2E). Additionally, some foraminifera shells exhibit complete or partial alteration, showing a reddish-yellow colour (Figs. 2F, G). Despite this pyritization or Fe-S mineralisation process, the pyritized foraminiferal tests remain intact and well-preserved.

Various morphological forms of pyrite, including framboids and patches, have been identified in the analyzed samples. These framboidal pyrites appear to coat or infill the chambers of foraminifera and are most commonly observed in the middle Pleistocene samples (Fig. 3). The framboids are characterized as spherical clusters of pyrite microcrystals (Figs. 3A-F). The small individual crystals inside a framboid appear to be well-developed and were observed inside the broken chambers of Trilobatus quadrilobatus (Figs. 3C, F). The interiomarginal aperture of Globorotalia hirsuta appears to be infilled with aggregates of uniform framboids (Figs. 3D-F). The chambers of the benthic foraminiferal species Bulimina striata are coated with irregular, loosely aggregated pyrite microcrystals, and the framboids in these samples are less well developed (Figs. 3G-I). Framboidal pyrite within the broken chamber of foraminiferal tests suggests in-situ authigenic mineralisation (Figs. 3J, K). The BSE images of polished thin sections for the sample at ~0.898 Ma reveal the cross-section of foraminiferal tests embedded in sediment, partially infilled with the framboidal pyrite (Fig. 3L). Dense concentrations of pyrite framboids tightly packed within the test (Fig. 3M). Framboids observed within broken foraminiferal chambers and the microcrystals inside them appear well-developed, likely because of the larger available space for their growth (Sawlowicz, 2000).

Flaky or patchy pyrite is observed as being coated on the external surfaces of foraminiferal chambers, particularly in specimens of *Neogloboquadrina humerosa* and *Sphaeroidinellopsis seminulina* (Figs. 4A-G) in the Upper Miocene samples. Irregular aggregates of pyrite microcrystals appear to infill chamber pores and are distributed along the sutures of *Dentoglobigerina altispira* (Figs. 4J-L). In the cross section, *Globorotalia menardii* tests are densely filled with the framboids, primarily near the inner layer of the shell (Fig. 4N). Some framboids appear deformed, accompanied by irregular pyrite aggregates on the broken skeletal fragments embedded in the sediments (Fig. 4O). The Fe-S coatings identified in this study exhibit diverse morphological characteristics. The results of the meta-analysis of framboid size measurements infer that the middle Pleistocene framboid population exhibits a smaller

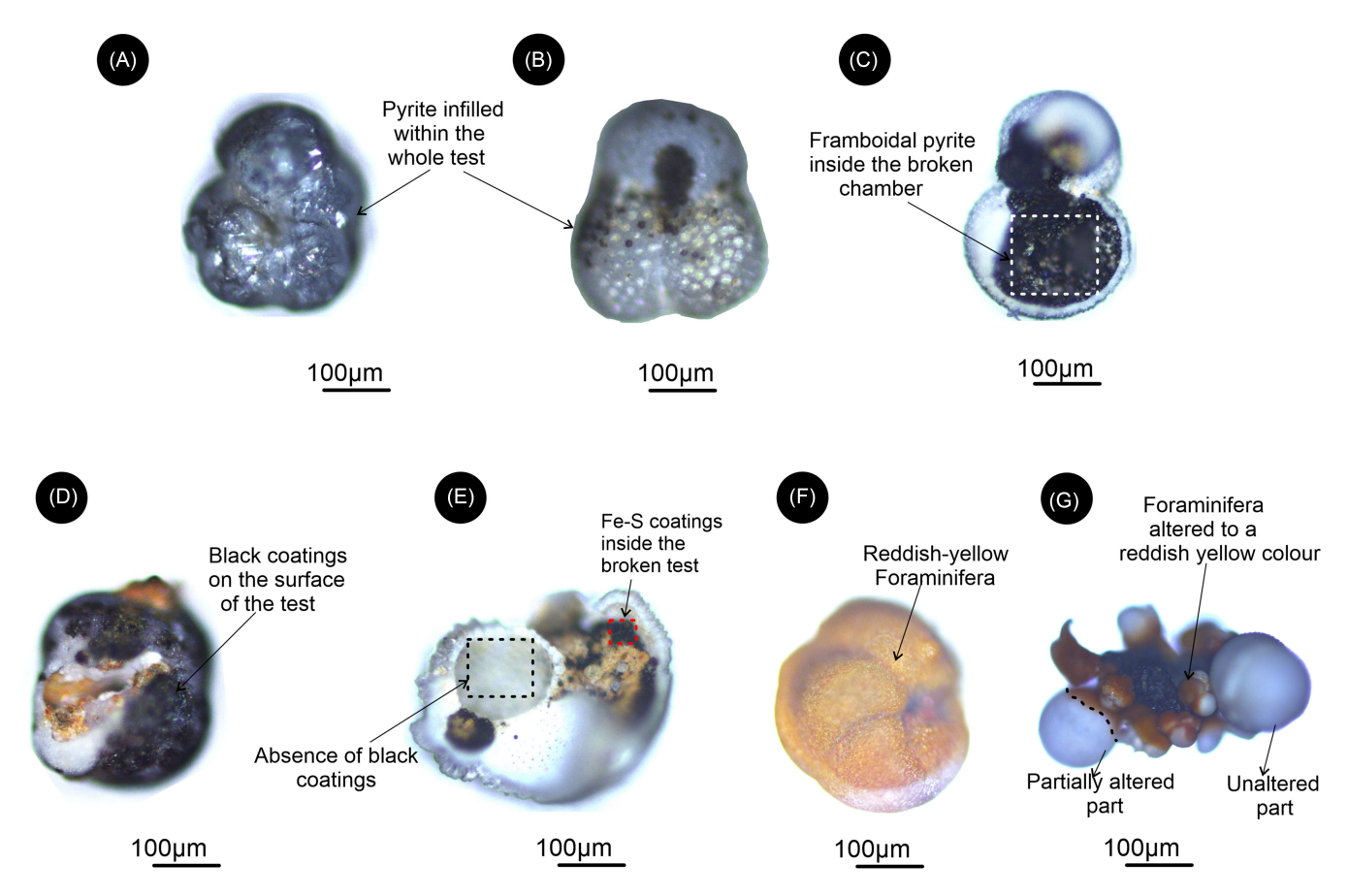


Figure 2. Representative photomicrographs of altered foraminifera. (A–C) Microscopic features observed from the Middle Pleistocene samples. (A) Foraminiferal shells appearing black due to internal infilling with Fe–S deposits; (B) Pyrite grows outward through the aperture after replacing the inside biological shells; (C) Broken chamber of a planktic foraminifera filled with framboidal pyrite. (D–G) Microscopic features observed from the Upper Miocene samples. (D) Black Fe–S coatings (patchy pyrite) on planktic foraminiferal tests; (E) Localized black Fe–S coatings on the internal side of broken shells, while within one chamber, while adjacent chambers remain unaltered within the broken fragments of the foraminifera; (F) Planktic foraminiferal shells completely altered (oxidized) to a reddish yellow colour; (G) Fe–S deposits surrounded by foraminifera and get altered through the point contact from the deposits. Photomicrographs are taken using an upright microscope (DMLM6000M) operating under visible light at IIT Kharagpur.

geometric mean diameter (~6.5  $\mu m)$ , whereas the Upper Miocene population shows a comparatively larger geometric mean diameter (~9.4  $\mu m)$  (Fig. S1).

# 4. b. Integrated geochemical investigations

# 4. b.1. Micro-Raman spectroscopy

The micro-Raman spectroscopy was conducted at eight points on different specimens to identify the iron sulphide phase in both framboidal and patchy morphologies. The spectra revealed characteristic peaks for the framboidal texture, with peaks at 341.4 cm<sup>-1</sup> (minor) and 375.4 cm<sup>-1</sup> (major), while the patchy coatings showed peaks at 339.3 cm<sup>-1</sup> (minor) and 375.2 cm<sup>-1</sup> (major), as depicted in Figure 5. These peaks, corresponding to the asymmetric bending (~340 cm<sup>-1</sup>) and symmetric stretching (~375-380 cm<sup>-1</sup>) modes of Fe-S bonds (Chen *et al.* 2022), confirm the presence of pyrite in both the morphologies.

## 4. b.2. SEM-EDS

The chemistry of iron sulphides associated with biogenic remains was analyzed using SEM-EDS to obtain a representative dataset. The elemental maps provide a semi-quantitative representation of Fe-S mineral phases and reveal additional elemental inclusions (Mg, Si, Al and Ni) within pyrite observed from the foraminiferal shells. Normalized atomic percentages of the detected elements were

obtained (supplementary Table 3) through the point analyses at positions i, ii and iii in the corresponding BSE images (Figs. 6-9). Unaltered foraminiferal chambers primarily consist of Ca, C and O, indicating a typical calcitic composition. Figure 6 displays the spatial distribution of Ca, Fe, S, Mg and Si in middle Pleistocene foraminiferal specimens, with Ca indicating the original calcareous shell composition, Fe and S aligning with framboidal pyrite locations and Mg and Si suggesting minor elemental incorporation. Figure 7 shows the chemistry of a sample at ~0.898 Ma, with abundant Ca along test walls, Fe and S indicating framboidal pyrite and Si, K and Al dispersed in the matrix, likely reflecting minor detrital or authigenic inclusions in the sediment. In the Upper Miocene samples, Fe and S are concentrated in pyrite patches on foraminiferal surfaces (Fig. 8), with weak Mg and Si signals suggesting minor admixtures in the sulphide assemblage. Notably, Ba as baryte on the surface of Sphaeroidinellopsis seminulina (Fig. 8L) may provide insights into diagenetic processes and depositional settings. Elemental mapping at ~6.58 Ma reveals the distribution of Ca, Fe, S, Si and Al in the sediment, with Fe and S maps showing association with specific microstructures and no evidence of calcite replacement in biogenic remains (Figs. 9B-F and H-L).

### 4. b.3. XRD analysis

The X-ray powder analysis (Fig. 10) was able to detect peaks corresponding to minerals with good crystallinity and higher

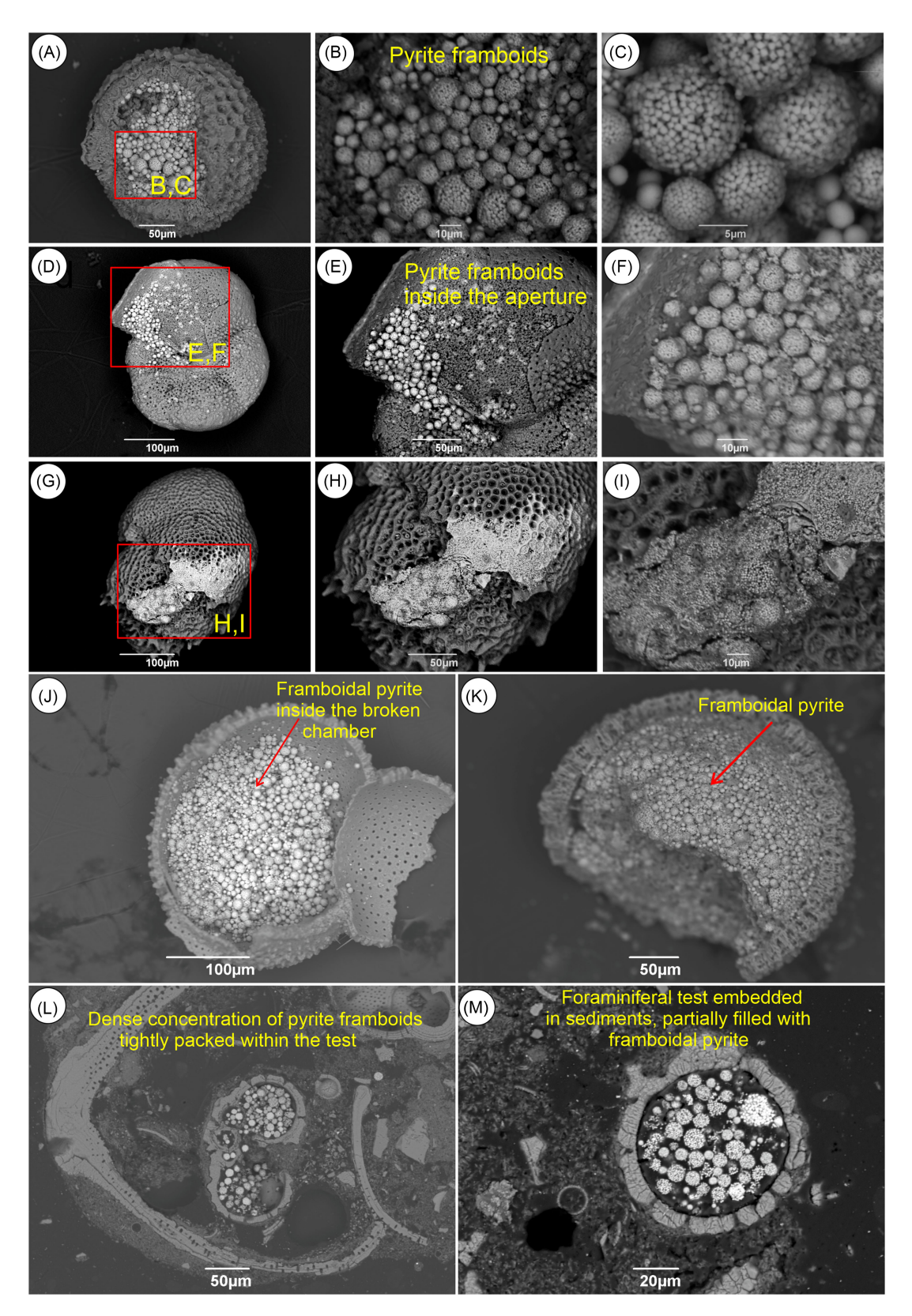


**Figure 3.** The following BSE images highlight the presence of framboidal pyrite in the Middle Pleistocene samples: (A–C) *Trilobatus quadrilobatus* exhibiting framboidal pyrite filling in its chambers; (D–F) *Globorotalia hirsuta* with framboidal pyrite in both the aperture and chambers; (G–I) *Bulimina striata* with irregular aggregates of pyrite crystals on its surface; (J, K) Framboidal pyrite found in the broken chambers of planktic foraminiferal shells; (L) Dense concentration of framboidal pyrites within foraminiferal tests, embedded in sediments; (M) Within the scattered sediment matrix, growth of framboids within foraminifera.

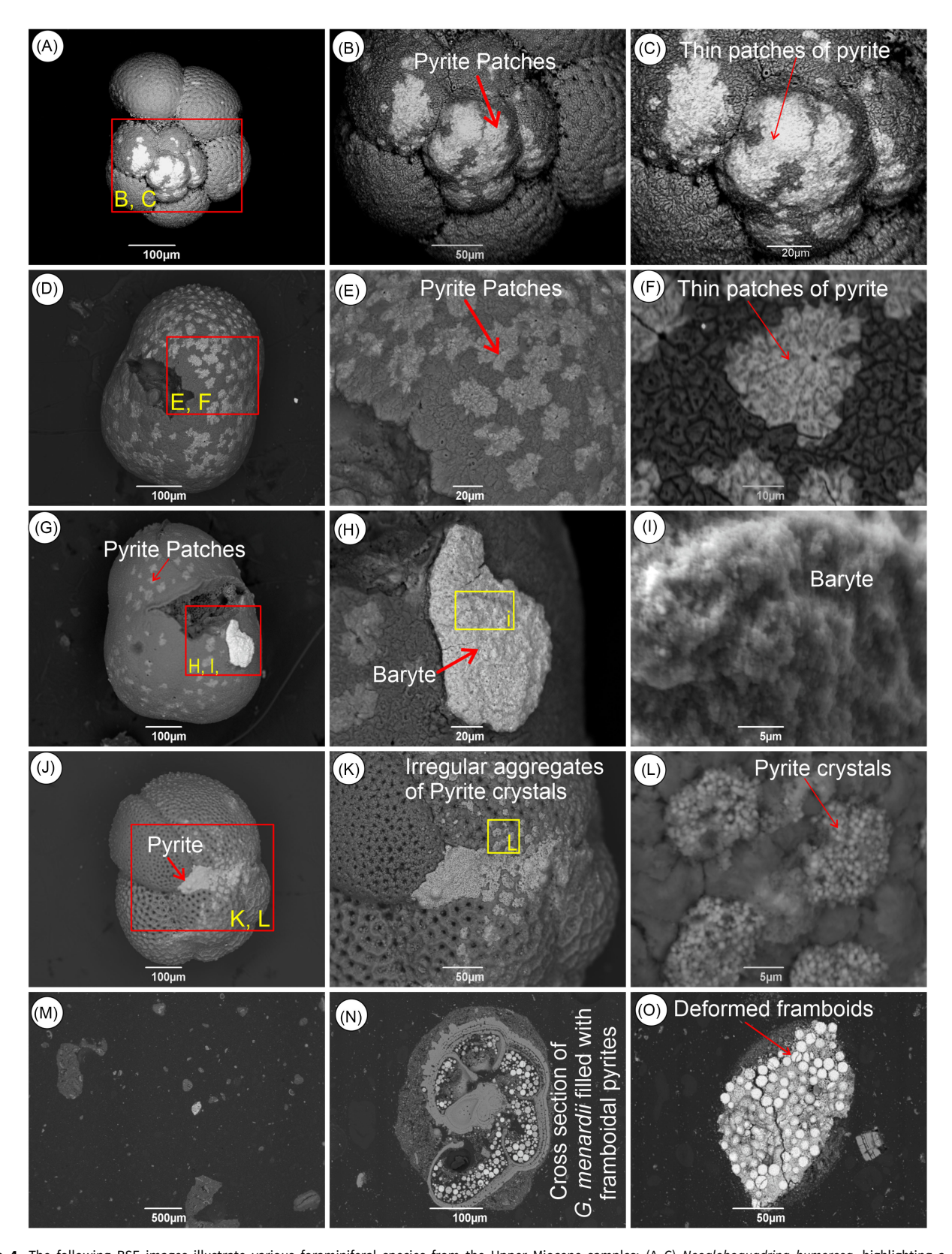


Figure 4. The following BSE images illustrate various foraminiferal species from the Upper Miocene samples: (A–C) Neogloboquadrina humerosa, highlighting a patchy distribution of pyrite; (D–F) Sphaeroidinellopsis seminulina, displaying patchy pyrite appearing to be coated on the test surface; (G–I) coexistence of pyrite patches and baryte on the surface of Sphaeroidinellopsis seminulina; (J–L) Dentoglobigerina altispira, exhibiting irregular aggregates of pyrite infilling the pores within its chambers. (M–O) Representative image for the sediment sample at ~6.58 Ma showcasing the tests and test fragments embedded within sediments; (N) cross-section of Globorotalia menardii filled with pyrite framboids; and (O) deformed and irregular aggregates of pyrite growth on a broken shell.

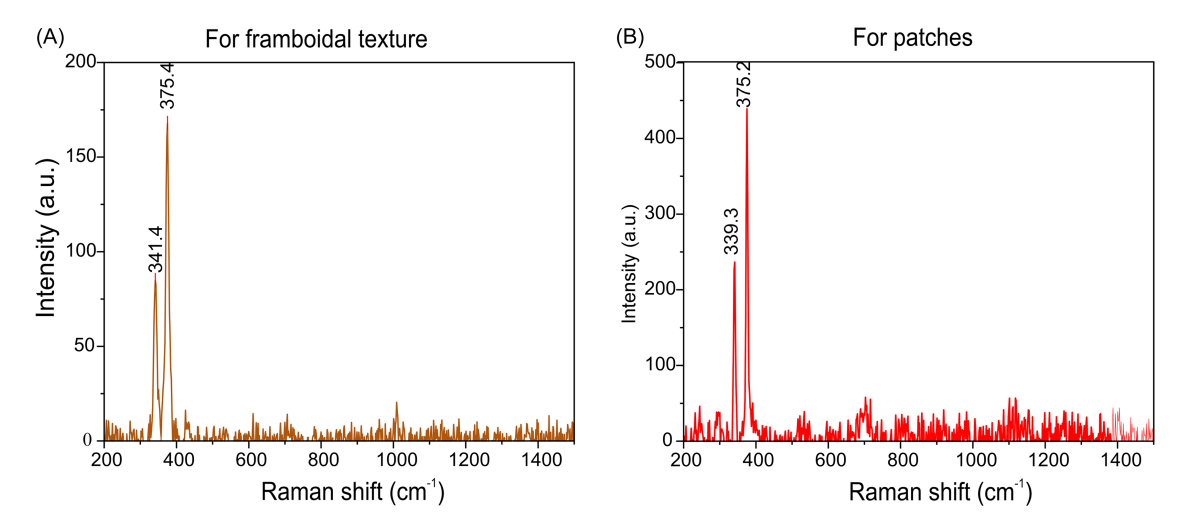


Figure 5. The Raman spectrum of the coatings observed on foraminiferal tests displays prominent peaks at ~375 and 340 cm<sup>-1</sup>, indicating the presence of the pyrite phase (after Lara et al. 2015). The spectrum is illustrated in two forms: (A) Raman spectra for framboidal pyrite and (B) Raman spectra for the patchy pyrite.

abundance, while the unidentified peaks represent minor mineral phases or poorly crystalline components. Sample at ~0.898 Ma was composed of three primary mineral phases: rutile (56%), chalcopyrite (25%) and quartz (19%); enstatite (53%) and quartz (47%) were primarily present in the sediment sample at ~1.07 Ma. The dominant presence of microcline (78%), along with quartz (28%), summarizes the mineral composition of the sample at ~6.58 Ma.

## 4. b.4. Stable isotope ratios

The  $\delta^{13}C$  values for both benthic and planktic foraminifera are illustrated in Figures 11A and 11B. The  $\delta^{13}C$  values in benthic foraminifera range from -0.1 to 0.5 ‰, with a mean value of 0.3 ‰. In contrast, planktic foraminifera show  $\delta^{13}C$  values ranging from 1.0 to 1.9 ‰, with an average of 1.5 ‰.

## 4. b.5. XRF analysis

The XRF analysis of sediment samples yielded phosphorus percentages (P%) and Fe/Mn ratios. Phosphorus concentrations averaged 0.02%, with maximum and minimum values of 0.027% and 0.017%, respectively (Figs. 11C, D). The average Fe/Mn ratio was found to be 56.2, with a maximum value of 112.4 recorded from the sample at  $\sim$ 1.06 Ma.

### 5. Discussion

At the study Hole, completely dark foraminiferal shells are absent in the Upper Miocene samples. Similarly, the reddish-yellow alterations and patchy surface coatings of pyrite seen in the Upper Miocene are not present in the middle Pleistocene samples. Based on distinct microtextural and morphological features of pyrite, framboid size distribution, variation in mineral composition and the burial depth, this study suggests the existence of diverse microenvironments in the southeastern Indian Ocean during the Upper Miocene and middle Pleistocene.

# 5. a. The mechanism of pyrite formation in the study area during the middle Pleistocene

The development of framboidal pyrite within foraminiferal tests in the deep-sea environments is principally driven by dissolved iron and the availability of organic matter, which drives the microbial activity under anoxic conditions (Canfield & Berner, 1987; Sawlowicz, 2000). The  $\delta^{13}$ C records of benthic and planktic foraminifera are widely used as proxies for nutrient availability and deep ocean paleocirculation (e.g., Mackensen & Bickert, 1999). The relatively low  $\delta^{13}$ C values of *Cibicides wuellerstorfii* and *Trilobatus* sacculifer indicate a period of high primary productivity in the southeastern Indian Ocean (Figs. 11A and 11B) during the middle Pleistocene, corroborated with the significant increase in relative abundances of Globigerina bulloides, a productivity-indicator species (Palei et al. 2024). This high productivity is likely driven by upwelling and increased organic matter flux contributing to bottom water column anoxia and anoxic conditions at the sediment-water interface. High phosphorus levels in bulk sediments (Fig. 11C), detected via XRF, further support anoxia, as phosphate-accumulating bacteria thrive in low oxygen (Kerrn-Jespersen & Henze, 1993). In addition to this, the elevated Fe/Mn ratio in Middle Pleistocene sediment samples (Fig. 11D) suggests anoxic conditions (Naeher et al. 2013). So, the past ocean oxygen deficiencies strongly rely on the palaeontological data along with the geochemical tracers (Raiswell, 2018). After the death of foraminifera, their shells descend to the ocean floor; upon settling on the ocean floor, the shells of foraminifera create comparatively confined microenvironments that restrict the material exchange between inside and outside of the organism (Chang et al. 2022). Microbial decomposition of soft tissues of foraminifera, facilitated by sulphate-reducing bacteria (SRB), produces H<sub>2</sub>S in oxygendepleted environments (Berner, 1985; Bosselmann, 2007; Szczepanik & Sawlowicz, 2010; Chen et al. 2021; Chang et al. 2022). Further, H<sub>2</sub>S reacts with available reactive iron sourced from dissolved seawater or iron-bearing minerals in the sediments (Berner, 1985; Szczepanik & Sawlowicz, 2010).

Iron is delivered to marine sediments through various processes, including fluvial, aeolian, submarine hydrothermal and glacial inputs. The middle Pleistocene period was marked by a transition to a more intense glacial cycle (Clark *et al.* 2006), likely enhancing the aridity in the regions adjacent to continents, including Northwest Australia (Christensen *et al.* 2017). This study infers the source of Fe content in southeastern Indian Ocean sediments was likely contributed by aeolian dust transport from Australian deserts, which are rich in iron-bearing, red sandstone

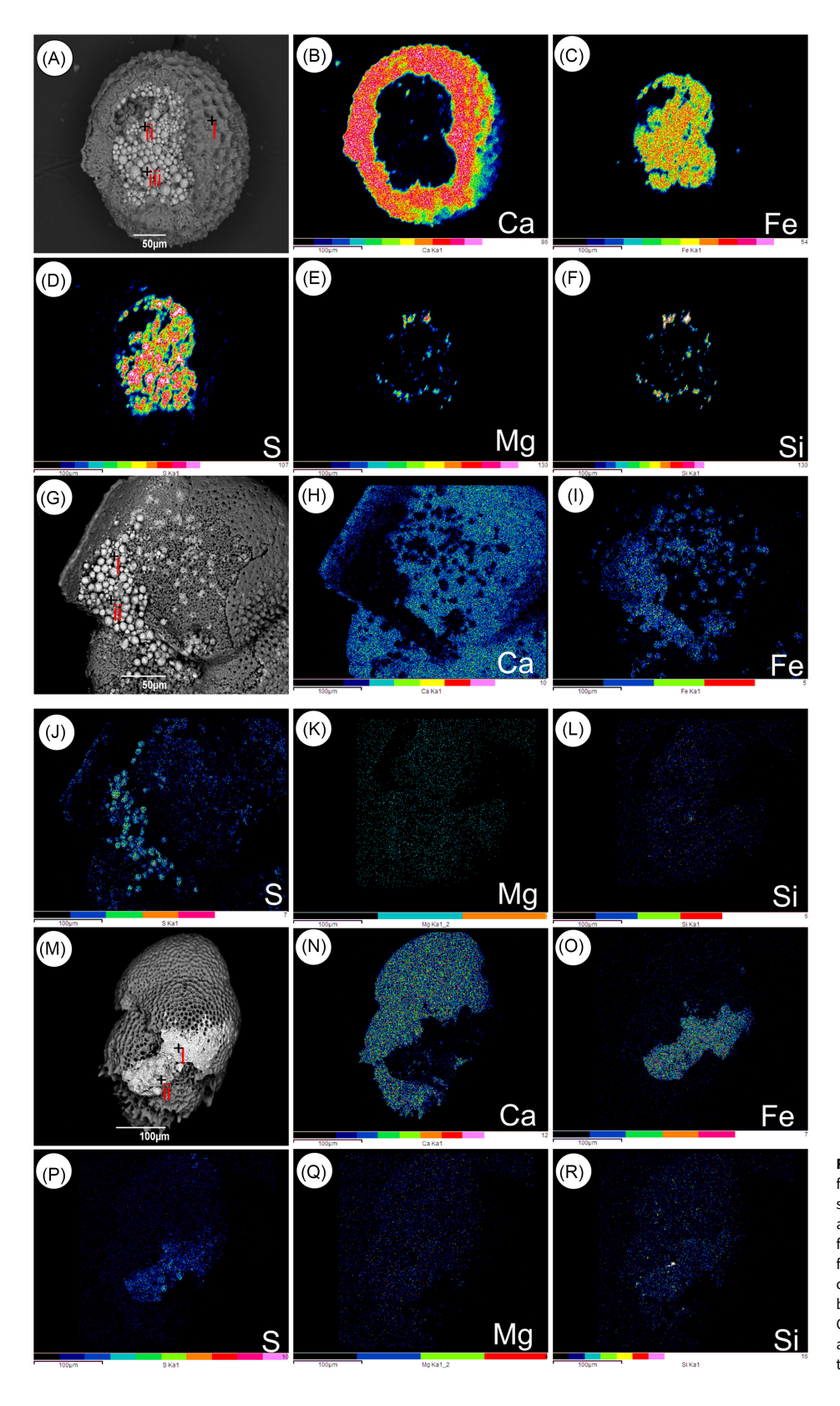


**Figure 6.** (A, G, M) Representative BSE images of foraminiferal tests from the Middle Pleistocene samples. (B–F) Chemical maps of Ca, Fe, S, Mg and Si corresponding to 'A'; (H–L) Ca, Fe, S, Mg and Si for 'G'; (N–R) Chemical maps of Ca, Fe, S, Mg and Si for 'M'. In these maps, colour intensity represents the concentration of each element at the pixel level, with black areas indicating elemental absence. (i, ii, iii) Corresponding semiquantitative atomic percentages obtained through point analysis (supplementary Table 3).

coatings (Stuut *et al.* 2019; Kuhnt *et al.* 2015). The labile Fe in aeolian can act as a micronutrient for phytoplankton and provides Fe ions that react with hydrogen sulphide reduced by SRB (Kenlee *et al.* 2024). Additionally, rutile, a dominant heavy mineral in the sample at ~0.898 Ma (Fig. 10A), was likely transported via dust

from distal sources, as no proximal fluvial settings (e.g., river mouths) favour its deposition. This study highlights the importance of aeolian dust from the Australian deserts for promoting Fe-S mineralisation in the study region. Elements such as Mg, Si, Al and Ni appear to be enriched; however, they may not

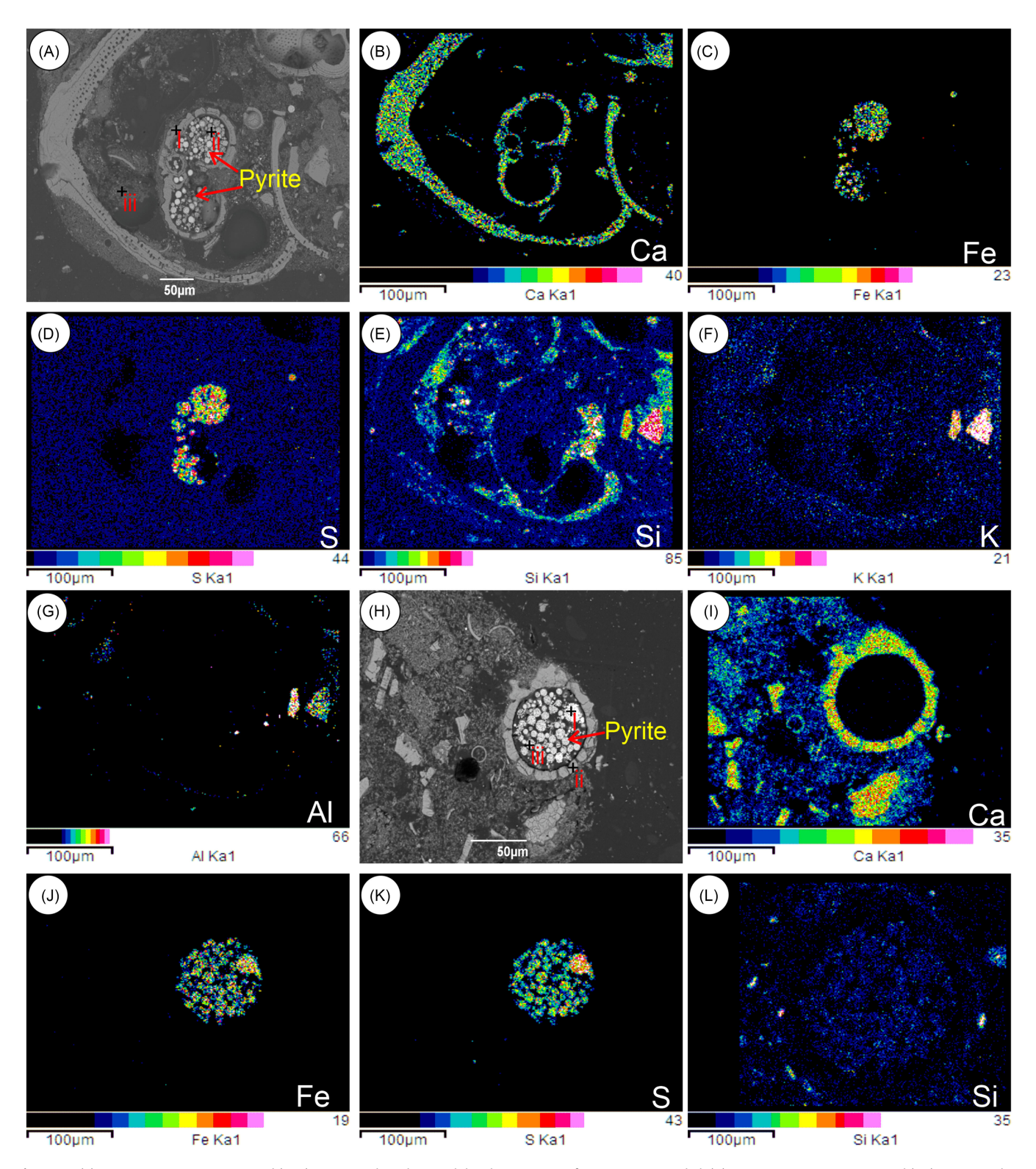


Figure 7. (A) Representative BSE image and (B–G) corresponding elemental distribution maps of Ca, Fe, S, Si, K and Al; (H) Representative BSE image and (I–L) corresponding elemental maps of Ca, Fe, S and Si illustrating sediment composition and Fe–S mineral deposits in the Middle Pleistocene sample at ~0.898 Ma.

be chemically bound to iron sulphide complexes. Instead, this enrichment might be associated with detrital mafic mineral grains, which are naturally enriched in compatible elements.

The presence of Ni within the pyrite texture (Fig. 6M (i, ii); supplementary Table 3) suggests reducing conditions in the

sediment. This scenario arises because redox-sensitive elements such as Ni, Cu, Zn and Cd are primarily delivered to sediments bound to organic matter. Following the decay of the organic matter, these elements can be retained in the sediment through association with pyrite during diagenesis (Tribovillard *et al.* 2006).

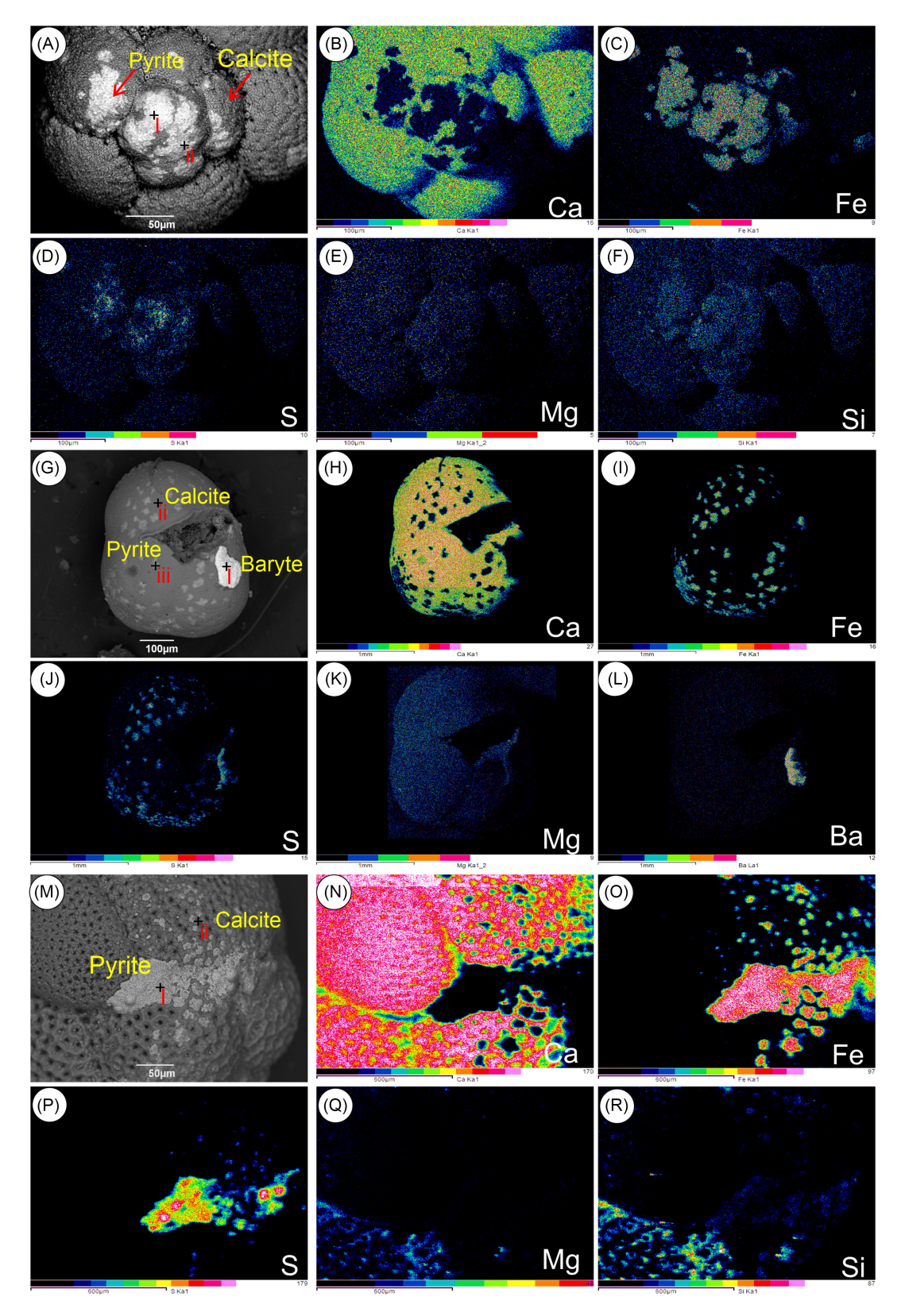


Figure 8. Chemical composition distribution maps. (A, G, M) Representative BSE images of foraminiferal tests from the Upper Miocene samples. (B–F) Ca, Fe, S, Mg and Si corresponding to 'A'; (H–L) Ca, Fe, S, Mg and Ba for 'G'; (N–R) Ca, Fe, S, Mg and Si for 'M'. Colour intensity in each elemental map reflects the relative concentration of the element at the pixel level, with black regions indicating the absence of the respective element. (i, ii, iii) The corresponding semiquantitative atomic percentages of elements, obtained through point analysis (supplementary Table 3).

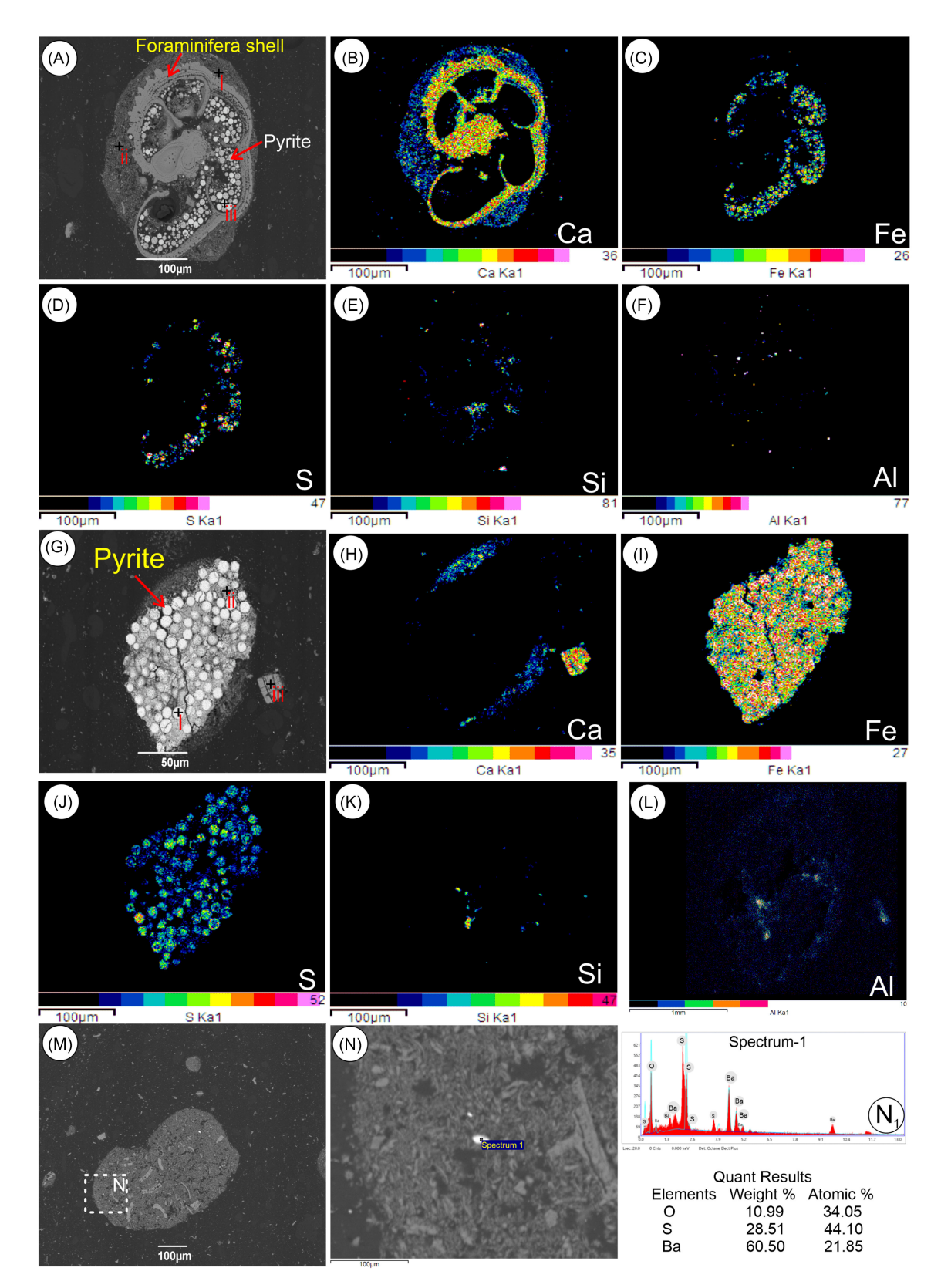
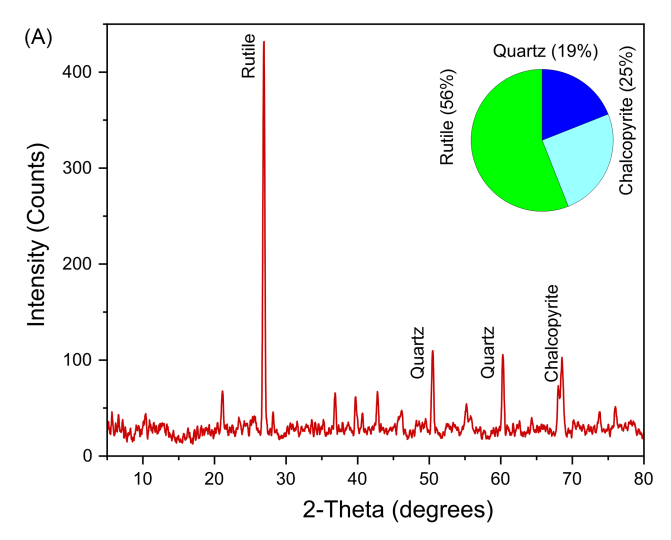
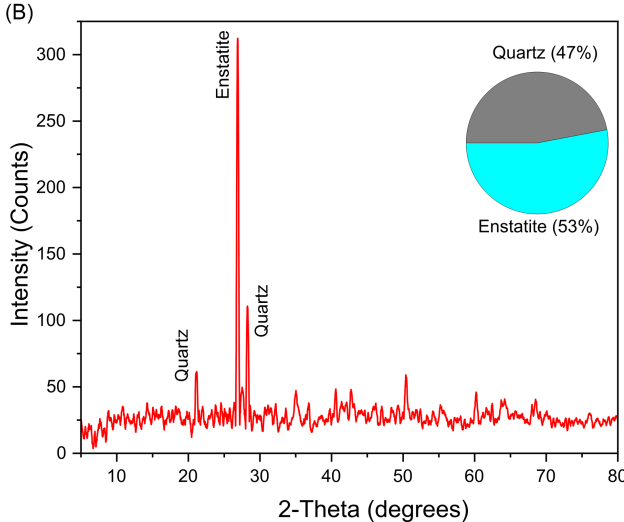
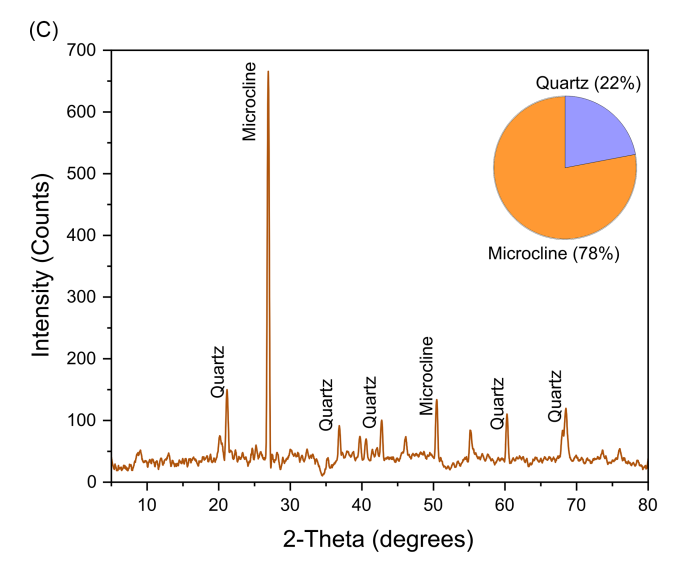


Figure 9. (A) Representative BSE image and (B–F) distribution of Ca, Fe, S, Si and Al corresponding to 'A'; (G) representative BSE image and (H–L) maps of Ca, Fe, S, Si and Al for 'G', showing the sediment's composition along with pyrite for the sample at ~6.58 Ma. (M, N) The presence of baryte within the sediment matrix.







**Figure 10.** The XRD patterns illustrate the mineralogical composition of bulk sediment samples. (A) Represents the mineral assemblage of the sample at  $\sim$ 0.898 Ma; (B) shows the composition of the sample at  $\sim$ 1.07 Ma; and (C) shows the mineral composition of the sample at  $\sim$ 6.58 Ma.

A box-and-whisker plot illustrating framboid size distribution shows that the middle Pleistocene samples contain well-preserved framboids, consistent with formation in anoxic porewaters during early diagenesis rather than in a euxinic water column (Fig. S1; Rickard, 2019).

# 5. b. Mechanism for the formation of pyrite at the study site during the Upper Miocene

The co-occurrence of oxidized foraminifera shells, framboidal pyrite and pyrite patches as coatings on the shells of foraminifera encountered in the Upper Miocene sediment samples suggests a complex interplay between the oxidising and localized reducing microenvironments in this study. Our multiproxy data reflect the reduced surface productivity in the Upper Miocene, inferred from the higher  $\delta^{13}$ C values in benthic and planktic foraminifera (Figs. 11A, B), along with lower P% and Fe/Mn ratios (Figs. 11C, D). The decline in productivity possibly limited the availability of organic matter and restricted the microbial processes, thus reducing sulphide availability. A comparatively low surface productivity and a low Fe/Mn ratio from XRF measurements of bulk marine sediments (Fig. 11) suggest the persistence of oxic conditions in the deep marine environments. The reddish-yellow colouration on foraminiferal shells is likely caused by the precipitation of iron oxides. This typically occurs under oxic conditions, where dissolved ferrous iron (Fe<sup>2+</sup>), commonly present in sediments, is oxidized to ferric iron (Fe<sup>3+</sup>) upon exposure to oxygen, leading to the formation of insoluble iron oxide minerals characterized by a reddish or yellow colour (Froelich et al. 1979).

However, the pyrite coatings on the tests and framboidal pyrite within the tests suggest localized microbial sulphate reduction might have occurred in the organic linings (Schieber, 2002). Additionally, the Upper Miocene framboids are comparatively sparse, irregular and less abundant, suggesting a predominantly diagenetic origin within the sediments (Fig. S1; Wilkin et al. 1996). The microbial activities depend on the organic matter type, porosity and skeletal structure openness (Sawlowicz, 2000) of the microorganism. The thin patches of pyrite observed on Neogloboquadrina humerosa and Sphaeroidinellopsis seminulina, which possess coarsely perforate test surfaces, conform closely to the surface structure, with the coarse perforations typically located at the center of the patches (Figs. 4C, F). The porous space may act as a localized reducing environments, concentrate microbial activity and promote patchy pyrite coatings, apparently driven by localized organic matter and iron availability (Canfield & Berner, 1987).

For pyrite formation, we consider enhanced terrigenous influx via riverine discharge as a possible source of Fe and other elemental inputs (Al, Mg, Si and Ba), possibly associated with increased humidity in northwestern Australia during the Upper Miocene (Groeneveld et al., 2017). The XRD analysis identifies microcline, a potassium feldspar, as the dominant mineral phase in the  $\sim$ 6.58 Ma sample, suggesting a regime of moderate chemical weathering. The presence of the baryte phase on the *Sphaeroidinellopsis seminulina* shells (Fig. 8G) and within aluminosilicate-rich marine sediments (Figs. 9M, N) may suggest a diagenetic origin. However, the absence of significant baryte enrichment rules out a hydrothermal source for this study (Buckman *et al.* 2020). Baryte likely precipitates in marine sediments when Ba<sup>2+</sup> and SO<sub>4</sub><sup>2-</sup> reach

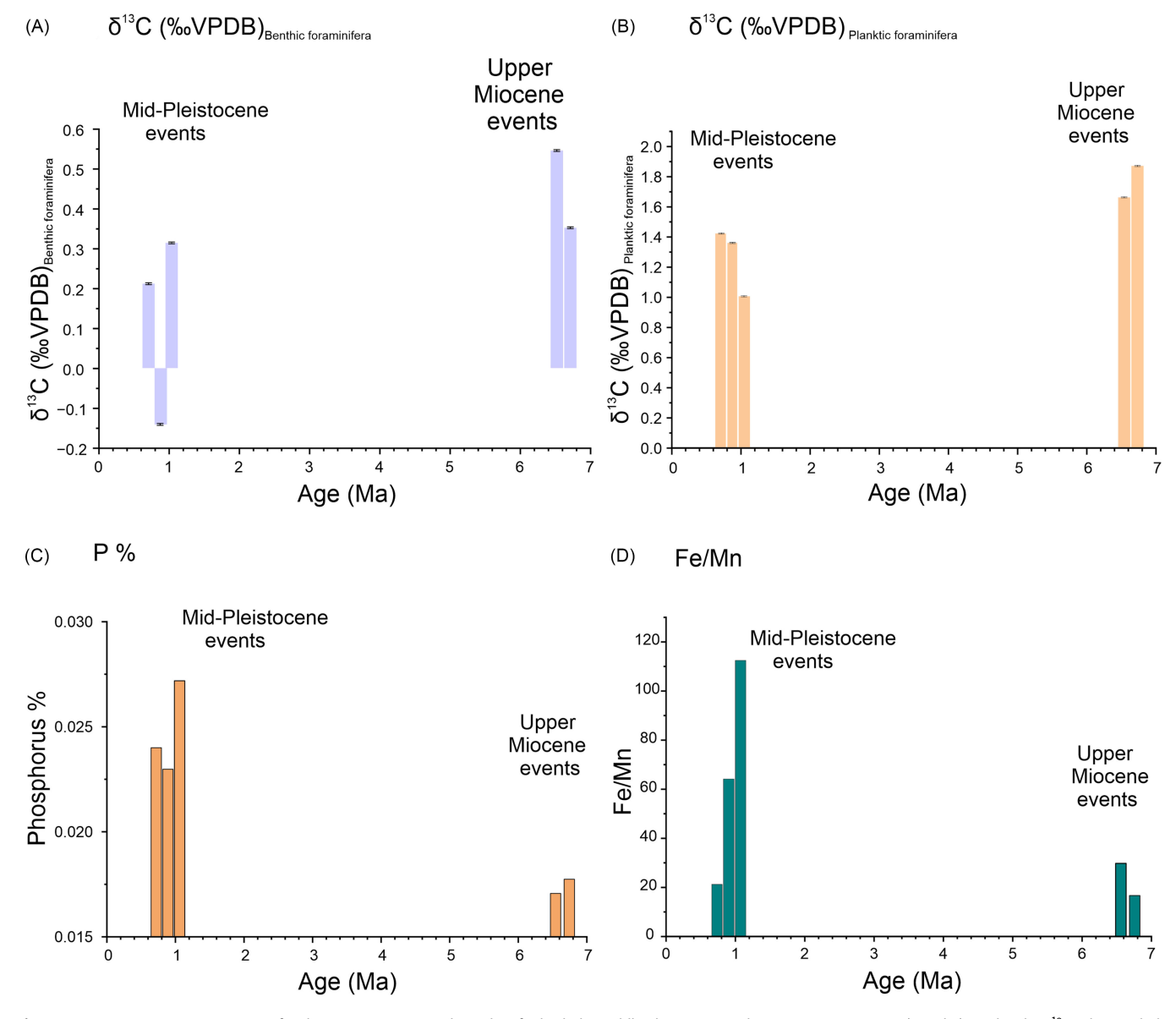


Figure 11. Histogram representation of carbon isotope ratios and XRF data for both the Middle Pleistocene and Upper Miocene events. (A and B) Display the  $\delta^{13}$ C values with the error bars (such as standard deviation) obtained from benthic and planktic foraminifera, respectively; (C and D) Present P (%) values and Fe/Mn ratios, respectively, derived from XRF analysis of bulk sediments.

saturation in pore waters, particularly in oxic to suboxic environments. Similar diagenetic baryte in planktonic tests from Tertiary marine sediments suggests in situ precipitation during post-burial (Stamatakis & Hein, 1993). This process often involves microbial sulphate reduction, where baryte dissolves and subsequently reprecipitates at redox boundaries where Ba-rich fluids encounter residual sulphate (Griffith & Paytan, 2012). These microenvironments likely developed within or near foraminiferal tests, enabling localized baryte formation. Barite likely formed in the upper, sulphate-rich sediment layer (Paytan & Griffith, 2007), while pyrite precipitated in localized anoxic micro-niches where SRB produced H<sub>2</sub>S (Canfield & Berner, 1987). Further studies, such as  $\delta^{34}$ S analysis of pyrite and baryte, are required. These will help to comment on whether pyrite initially precipitated within the porous spaces of foraminiferal tests or if diagenetic baryte formed later during post-burial sedimentary processes.

# 5. c. Palaeoceanographic implications from pyritized foraminifera

All the evidence discussed above collectively influences the formation and preservation of pyrite within foraminiferal tests at the study hole during the different geological time periods. The short-lived oxygen-deprived events inferred in this study are potentially driven by local microenvironmental changes rather than basin-wide anoxia. This is particularly intriguing at Hole 763A, where pulses of upwelling events are evident (Sinha & Singh, 2007; Palei et al. 2024) despite the dominance of the warm, oligotrophic, poleward-flowing Leeuwin Current and the absence of a persistent oxygen minimum zone. Our results suggest that anoxic bottom-water conditions and elevated Fe concentrations in sediments and pore waters likely promoted framboidal pyrite formation during the middle Pleistocene, a period marked by intensified global glacial cycles (Clark et al. 2006). Local anoxic

conditions, often resulting from high rates of organic matter decomposition, will promote the reduction of iron, fostering pyrite formation (Canfield, 1989). These framboids, associated with anoxic bottom-water conditions, most likely developed near the sediment-water interface, typically within a few centimetres of burial, during early diagenesis (Wilkin *et al.* 1996).

Patches and irregular aggregates of pyrite on foraminiferal shells indicate localized oxygen-depleted conditions, even though overall productivity was low and organic matter supply was limited. This contrasts with the uniform framboidal textures typical of persistently anoxic environments and highlights the importance of microenvironments in shaping pyrite morphology. Oxidising conditions at the sediment-water interface preserved unaltered tests, while downward shifting of the oxic-anoxic boundary during burial can modify the diagenetic pathways (Orsi et al. 2020). In deeper sediment layers, limited reactive iron and accumulated hydrogen sulphide promoted framboid development within foraminiferal chambers, where SRB thrived locally (Wang & Morse, 1996). These features suggest that Upper Miocene foraminiferal pyritization in the southeastern Indian Ocean occurred during late-stage diagenesis and might have been influenced by strong thermohaline circulation or bioturbation that modified bottom-water oxygenation. The mechanism for the formation of different types of pyrites under variable bottom water conditions is illustrated in Figure S2.

#### 6. Conclusions

We report the contrasting morphology and microtextures of pyrite associated with foraminiferal tests retrieved from ODP Hole 763A located in the Southeastern Indian Ocean. The contrasting microtextures and morphology of pyrite might be linked to variations in sedimentary conditions, diagenetic processes and bottom water oxygenation over time in deep-sea core sediments. Based on the evidence discussed above, the middle Pleistocene foraminiferal tests predominantly display well-developed framboidal pyrite textures, suggesting stable anoxic conditions during early diagenesis. These anoxic conditions in the southeastern Indian Ocean in the middle Pleistocene were potentially driven by high surface productivity and aeolian dust, which supplied sedimentary iron and biological nutrients to bottom waters. In contrast, the pyrite morphology in the late Miocene samples suggests the existence of localized reducing microenvironments, as evidenced by pyrite patches on foraminiferal tests, despite predominantly oxic bottom-water conditions. These microenvironments were likely formed due to microbial activity or organic matter decomposition within the foraminiferal tests rather than reflecting basin-wide anoxia. This study provides insights into the practical use of pyritized microfossils as a paleoceanographic proxy in deep-sea environments, as diagenetic pyrite is closely associated with organic matter and its oxygenation in bottom water and, in turn, with ocean productivity and deep circulation systems. Further investigations involving trace element analysis and  $\delta^{34}$ S isotopic signatures of pyrite within foraminiferal tests could help reveal distinct geochemical conditions and pathways associated with its genesis.

**Supplementary material.** The supplementary material for this article can be found at https://doi.org/10.1017/S0016756825100307.

**Acknowledgements.** The authors thank the IODP Kochi Core Centre for providing samples (request no. #75666IODP). Indian Institute of Technology

Kharagpur is thankfully acknowledged for giving fellowships to RRP to carry out this study. AKG thanks the Anusandhan National Research Foundation (earlier Science and Engineering Research Board or SERB), Department of Science and Technology, Government of India, for the Sir J. C. Bose fellowship (Grant No. JBR/2021/000019) to support this study. The authors thank Zbigniew Sawlowicz, an anonymous reviewer and Editor Peter Clift for their valuable and constructive comments, which have greatly improved the clarity and quality of the original manuscript.

**Competing interests.** The authors state that they do not have any known competing financial interests or personal ties that could appear to have influenced the work reported in this study.

#### **References**

- Berner RA (1984) Sedimentary pyrite formation: an update. Geochimica et cosmochimica Acta 48(4), 605–15. http://dx.doi.org/10.1016/0016-7037(84) 90089-9
- Berner RA (1985) Sulphate reduction, organic matter decomposition and pyrite formation. Philosophical Transactions of the Royal Society of London. Series A, Mathematical and Physical Sciences 315(1531), 25–38. https://doi.org/10.1098/rsta.1985.0027
- Buckman J, Mahoney C, März C and Wagner T (2020) The secret 'after life' of foraminifera: Big things out of small. Minerals 10(6), 550. https://doi.org/10.3390/min10060550
- **Bosselmann** K (2007) Sulfate reduction and iron-manganese cycling in intertidal surface sediments of the southern North Sea (Doctoral dissertation, Universität Oldenburg).
- Canfield DE and Berner RA (1987) Dissolution and pyritization of magnetite in anoxic marine sediments. *Geochimica et Cosmochimica Acta* 51(3), 645–59. https://doi.org/10.1016/0016-7037(87)90076-7
- Canfield DE (1989) Reactive iron in marine sediments. Geochimica et Cosmochimica Acta 53(3), 619–32. https://doi.org/10.1016/0016-7037(89)
- Chang J, Li Y and Lu H (2022) The morphological characteristics of authigenic pyrite formed in marine sediments. *Journal of Marine Science and Engineering* 10(10), 1533. https://doi.org/10.3390/jmse10101533
- Chen X, Sun X, Wu Z, Liao J and Chen H (2021) Formation of Fe-Mn coatings on foraminifera from the ultraslow-spreading southwest Indian Ridge: implications for hydrothermal and diagenetic overprints in sediments. Ore Geology Reviews 138, 104377. https://doi.org/10.1016/j.oregeorev.2021.104377
- Chen J, Li H, Yuan Y, Zhang M, Shuai S and Wan J (2022) Raman spectroscopic studies of pyrite at high pressure and high temperature. *Minerals* 12(3), 332. https://doi.org/10.3390/min12030332
- Christensen BA, Renema W, Henderiks J, Vleeschouwer DD, Groeneveld J, Castañeda IS, Reuning L, Bogus K, Auer G, Ishiwa T, McHugh CM, Gallagher SJ and Fulthorpe CS (2017) Indonesian Throughflow drove Australian climate from humid Pliocene to arid Pleistocene. *Geophysical Research Letters* 44(13), 6914–25. https://doi.org/10.1002/2017GL072977
- Clark PU, Archer D, Pollard D, Blum JD, Rial JA, Brovkin V, Mix AC, Pisias NG and Roy M (2006) The middle Pleistocene transition: characteristics, mechanisms, and implications for long-term changes in atmospheric pCO2. Quaternary Science Reviews 25(23-24), 3150-84. https://doi.org/10.1016/j.quascirev.2006.07.008
- Emmings JF, Poulton SW, Walsh J, Leeming KA, Ross I and Peters SE (2022)

  Pyrite mega-analysis reveals modes of anoxia through geological time.

  Science Advances 8(11), eabj5687. https://doi.org/abj5687
- Froelich P, Klinkhammer G, Bender M, Luedtke N, Heath G, Cullen D, Dauphin P, Hammond D, Hartman B and Maynard V (1979) Early oxidation of organic matter in pelagic sediments of the eastern equatorial Atlantic: Suboxic diagenesis. *Geochimica et Cosmochimica Acta* 43(7), 1075–90. https://doi.org/10.1016/0016-7037(79)90095-4
- Gibbons AD, Barkhausen U, Bogaard PVD, Hoernle K, Werner R, Whittaker JM and Muller RD (2012) Tectonic evolution of the West Australian margin. *Geochemistry, Geophysics, Geosystems* 13, 1–25. https://doi.org/10.1029/2011GC003919

- Griffith EM and Paytan A (2012) Barite in the ocean occurrence, geochemistry and palaeoceanographic applications. Sedimentology 59(6), 1817–35. https://doi.org/10.1111/j.1365-3091.2012.01327.x
- Groeneveld J, Henderiks J, Renema W, McHugh CM, Vleeschouwer DD, Christensen BA, Fulthorpe CS, Reuning L, Gallagher SJ, Bogus K, Auer G and Ishiwa T (2017) Australian shelf sediments reveal shifts in Miocene Southern Hemisphere westerlies. *Science Advances* 3(5), e1602567. https://doi.org/1602567
- Gupta AK and Thomas E (2003) Initiation of Northern Hemisphere glaciation and strengthening of the northeast Indian monsoon: ocean drilling program site 758, eastern equatorial Indian Ocean. Geology 31(1), 47–50. https://doi.org/10.1130/00917613(2003)031<0047:IONHGA>2.0.CO;2
- Haq BU and von Rad U, (1990) Proceeding of ODP Initial Report 122: Site 763.
  College Station, TX. https://doi.org/10.2973/odp.proc.ir.122.109.1990.
- Hoogakker BA, Davis C, Wang Y, Kusch S, Nilsson-Kerr K, Hardisty DS, ... and Zhou Y (2025) Reviews and syntheses: review of proxies for low-oxygen paleoceanographic reconstructions. *Biogeosciences* 22(4), 863–957.
- Imai N, Terashima S, Itoh S and Ando A (1996) 1996 compilation of analytical data on nine GSJ geochemical reference samples, "Sedimentary rock series". Geostandards Newsletter 20(2), 165–216.
- Schieber J (2002) Sedimentary pyrite: a window into the microbial past. *Geology* **30**(6), 531–34. https://doi.org/10.1130/0091-7613(2002)030<0531:SPAWIT>2. 0.CO:2
- Karp AT, Andrae JW, McInerney FA, Polissar PJ and Freeman KH (2021) Soil carbon loss and weak fire feedback during Pliocene C4 grassland expansion in Australia. *Geophysical Research Letters* **48**(2), e2020GL090964. https://doi.org/10.1029/2020GL090964
- Kenlee B, Owens JD, Raiswell R, Poulton SW, Severmann S, Sadler PM and Lyons TW (2024) Long-range transport of dust enhances oceanic iron bioavailability. Frontiers in Marine Science 11, 1428621. https://doi.org/ 10.3389/fmars.2024.1428621
- Kerrn-Jespersen JP and Henze M (1993) Biological phosphorus uptake under anoxic and aerobic conditions. Water Research 27(4), 617–24. https://doi. org/10.1016/0043-1354(93)90171-D
- Kuhnt W, Holbourn A, Xu J, Opdyke B, De Deckker P, Röhl U and Mudelsee M (2015) Southern Hemisphere control on Australian monsoon variability during the late deglaciation and Holocene. *Nature Communications* 6(1), 5916. doi:10.1038/ncomms6916(2015).
- Lara RH, Monroy MG., Mallet M, Dossot M, González MA, Cruz R. (2015)
  An experimental study of iron sulfides weathering under simulated calcareous soil conditions. *Environmental Earth Sciences* 73, 1849–69.
- Lee H, Jo K, Baek S, Kwon KD, Son S, Lee HS, Gang N and Kim Y (2024)
  Occurrence characteristics of authigenic pyrite in the deep-sea environment and its paleoceanographic implications based on core sediments from IODP Expedition 342 Site U1406. Palaeogeography, Palaeoclimatology, Palaeoecology 655, 112535. https://doi.org/10.1016/j.palaeo.2024.112535
- Mackensen A and Bickert T (1999) Stable carbon isotopes in benthic foraminifera: proxies for deep and bottom water circulation and new production. In *Use of proxies in paleoceanography: Examples from the South Atlantic* pp. 229–54. Berlin, Heidelberg: Springer Berlin Heidelberg.
- Stamatakis MG and Hein JR (1993); Origin of barite in Tertiary marine sedimentary rocks from Lefkas Island, Greece. *Economic Geology* 88(1), 91–103. https://doi.org/10.2113/gsecongeo.88.1.91
- Naeher S, Gilli A, North RP, Hamann Y and Schubert CJ (2013) Tracing bottom water oxygenation with sedimentary Mn/Fe ratios in Lake Zurich, Switzerland. Chemical Geology 352, 125–33. https://doi.org/10.1016/j.che mgeo.2013.06.006
- Ohfuji H and Rickard D (2005) Experimental syntheses of framboids—a review. *Earth-Science Reviews* 71(3-4), 147–70. https://doi.org/10.1016/j.earscirev.2005.02.001
- Orsi WD, Morard R, Vuillemin A, Eitel M, Wörheide G, Milucka J and Kucera M (2020) Anaerobic metabolism of Foraminifera thriving below the seafloor. *The ISME Journal* 14(10), 2580–94. https://doi.org/10.1038/s41396-020-0708-1
- Palei RR, Gupta AK, Sanyal P and Jaiswal MK (2024) Leeuwin current dynamics in the SE Indian Ocean and implications for regional surface hydrography since

- the latest Miocene: Results from ODP Site 763A. *Global and Planetary Change* 237, 104459. https://doi.org/10.1016/j.gloplacha.2024.104459
- Paytan A and Griffith EM (2007) Marine barite: recorder of variations in ocean export productivity. Deep Sea Research Part II: Topical Studies in Oceanography 54(5-7), 687–705. https://doi.org/10.1016/j.dsr2.2007.01.007
- Poulton SW, Krom MD and Raiswell R (2004) A revised scheme for the reactivity of iron (oxyhydr)oxide minerals towards dissolved sulfide. Geochimica et Cosmochimica Acta 68(18), 3703–15. https://doi.org/ 10.1016/j.gca.2004.03.012
- Raiswell R, Hardisty DS, Lyons TW, Canfield DE, Owens JD, Planavsky NJ, ... and Reinhard CT (2018) The iron paleoredox proxies: a guide to the pitfalls, problems and proper practice. *American Journal of Science* 318(5), 491–526.
- Raffi I, Wade BS, Pälike H, Beu AG, Cooper R, Crundwell MP and Vernyhorova YV (2020) The Neogene period. In *Geologic Time Scale 2020*. pp. 1141–215. Elsevier https://doi.org/10.1016/B978-0-12-824360-2.00029-2
- Rickard D (2019) Sedimentary pyrite framboid size-frequency distributions: a meta-analysis. Palaeogeography, Palaeoclimatology, Palaeoecology 522, 62–75. https://doi.org/10.1016/j.palaeo.2019.03.010
- Rickard D (2021) Framboids. Oxford University Press, New York.
- Sinha DK and Singh AK (2007) Episodes of weakening of Leeuwin current (Southeast Indian Ocean) during quaternary: isotopic and planktic foraminiferal evidences. *Micropaleontology: Application in Stratigraphy and Paleoceanography* 305.
- Snowdon LR and Meyers PA (1992) Source and maturity of organic matter in sediments and rocks from Sites 759, 760, 761, and 764 (Wombat Plateau) and Sites 762 and 763 (Exmouth Plateau). Proceedings of the Ocean Drilling Program, Scientific Results, Leg 122, Exmouth Plateau, 122, 309–315.
- Stagg HMJ and Colwell JB (1994) The Structural Foundations of the Northern Carnarvon Basin. In The sedimentary basins of Western Australia: Proceedings of petroleum exploration society of Australia symposium, Perth (pp. 349–72).
- Stuut BW, Deckker PD, Saavedra-Pellitero M, Bassinot F, Drury AJ, Walczak MH, Nagashima K and Murayama M (2019) A 5.3-Million-year history of monsoonal precipitation in Northwestern Australia. *Geophysical Research Letters* 46(12), 6946–54. https://doi.org/10.1029/2019GL083035
- Sawlowicz Z (2000) Framboids: from their origin to application. *Prace Mineralogiczne* 88, 1–80.
- Szczepanik P and Sawlowicz Z (2010) Fe-S mineralization in the Jurassic biogenic remains (Częstochowa, Poland). *Geochemistry* **70**(1), 77–87. https://doi.org/10.1016/j.chemer.2009.10.003
- Tribovillard N, Algeo T J, Lyons T and Riboulleau A (2006) Trace metals as paleoredox and paleoproductivity proxies: an update. *Chemical Geology* **232**(1-2), 12–32. https://doi.org/10.1016/j.chemgeo.2006.02.012
- Upadhyay MK, Majumdar A, Barla A, Bose S and Srivastava S (2021)
  Thiourea supplementation mediated reduction of grain arsenic in rice (Oryza sativa L.) cultivars: A two-year field study. *Journal of Hazardous Materials* 407, 124368. https://doi.org/ 10.1016/j.jhazmat.2020.124368.
- Wang X, Zhang J, Shi M, Pang Y, Zhao Y and Yang X (2023) Changing hydrocarbon-producing potential of the Cambrian niutitang shale: insights from pyrite morphology and geochemical characteristics. ACS Omega 8(7), 7172. https://doi.org/10.1021/acsomega.3c00174
- Wang Q and Morse JW (1996) Pyrite formation under conditions approximating those in anoxic sediments I. Pathway and morphology. *Marine Chemistry* 52(2), 99–121. https://doi.org/10.1016/0304-4203(95)00082-8
- Wignall PB, Newton R and Brookfield ME (2005) Pyrite framboid evidence for oxygen-poor deposition during the Permian–Triassic crisis in Kashmir. Palaeogeography, Palaeoclimatology, Palaeoecology 216(3-4), 183–88. https://doi.org/10.1016/j.palaeo.2004.10.009
- Wilkin RT, Barnes HL and Brantley SL (1996) The size distribution of framboidal pyrite in modern sediments: an indicator of redox conditions. *Geochimica et cosmochimica acta* **60**(20), 3897–912. https://doi.org/10.1016/0016-7037(96)00209-8
- Wilkin RT, Arthur MA and Dean WE (1997) History of water-column anoxia in the Black Sea indicated by pyrite framboid size distributions. *Earth and Planetary Science Letters* 148, 517–25. https://doi.org/10.1016/S0012-821X(97)00053-8